ADVANCED FUNCTIONAL MATERIALS
www.afm-journal.de

Noise-Assisted Crystallization of Opal Films

Worawut Khunsin, Andreas Amann, Gudrun Kocher-Oberlehner, Sergei G. Romanov, Saroj Pullteap, Han Cheng Seat, Eoin P. O'Reilly, Rudolf Zentel, and Clivia M. Sotomayor Torres**

An improvement of the crystal quality of opal films self-assembled from polymer spheres in a moving meniscus using the agitation by white noise acoustic vibrations is demonstrated. A tenfold higher ordering of a hexagonal sphere packing in the (111) plane is achieved. This crystallization method, the mechanism of which is described in terms of the stochastic resonance, is a contrast to the widely used approach based on maintaining equilibrium conditions during the crystallization process. The precise quantification of the incremental lattice order improvement as a function of acoustic noise intensity is achieved by calculating the probability of finding an opposite partner for each sphere in the lattice. This method is examined against conventional and established techniques such as Fourier transforms and translational and bond-orientational correlation functions, and its advantages are demonstrated. Rotational symmetry analysis of diffraction resonances in measured and calculated optical transmission spectra as a function of the azimuth lattice orientation are carried out to confirm that the surface ordering translates into the bulk ordering of high index crystal planes, which are most sensitive to disorder.

1. Introduction

Photonic crystals (PhCs) have been extensively studied for the past two decades as a unique platform to understand light–matter interactions in complex media.[1–4] Additionally, the fascinating optical properties of PhCs have been exploited in industrially relevant applications such as high sensitivity sensors[5–7] and enhanced solar cells.[8–10] It is commonly accepted that the ultimate PhC performance can be achieved with perfectly ordered 3D structures. Among several techniques used for 3D PhC fabrication, colloidal crystals in general, and opals in particular, stand out for their preparation simplicity and compatibility with Si platforms,[11] making them the most widely studied 3D PhCs to date. However, the self-assembled structures suffer from the distractive influence of various structural defects,[12,13] which

Dr. W. Khunsin, Dr. A. Amann, Prof. E. P. O'Reilly
Tyndall National Institute
Lee Maltings, Cork, Ireland
E-mail: worawut.khunsin@icn.cat
Dr. W. Khunsin, Prof. C. M. Sotomayor Torres
Catalan Institute of Nanotechnology (ICN-CIN2)
Campus UAB, 08193 Bellaterra (Barcelona), Spain
E-mail: clivia.sotomayor@icn.cat
Dr. A. Amann
School of Mathematical Sciences
University College Cork, Ireland
Dr. G. Kocher-Oberlehner,
Division of Biomedical Engineering
School of Engineering
University of Glasgow
Rankine Building, Oakfield Avenue, Glasgow, G12 8LT, UK
Dr. S. G. Romanov
Institute of Optics
Information and Photonics
University of Erlangen-Nuremberg
Günther-Scharowsky-Str. 1, 91058 Erlangen, Germany
Dr. S. G. Romanov
Ioffe Physical Technical Institute RAS
194021, Polithekhnicheskaya ul., 26, St. Petersburg, Russia
Dr. S. Pullteap
Department of Mechanical Engineering
Faculty of Engineering and Industrial Technology
Silpakorn University
Nakhon Pathom 73000 Thailand
Dr. S. Pullteap, Dr. H. C. Seat
Université de Toulouse
INP; LASS, CNRS, F-31077 Toulouse, France
Prof. E. P. O'Reilly
Department of Physics
University College Cork, Ireland
Prof. R. Zentel
Institute of Organic Chemistry
Johannes Gutenberg University Mainz
Düsbergweg 10-14, D-55099 Mainz, Germany
Prof. C. M. Sotomayor Torres
Catalan Institute of Research and Advanced Studies
ICREA, 08010 Barcelona, Spain
Prof. C. M. Sotomayor Torres
Dept. of Physics
UAB, 08193 Bellaterra (Barcelona), Spain

DOI: 10.1002/adfm.201102605

are detrimental to the formation of the photonic bandgap (PBG).[14]

Thus, research towards improving the ordering of opal PhCs is essential. Most research effort in this direction is based on purely chemical methods that focused on establishing the ordered colloidal configuration in the liquid phase and careful translation of this ordered architecture onto a solid substrate. However, one can imagine an alternative strategy that engages the stochastic mechanism of the ensemble formation.This method uses many attempts by the ensemble to realize the most energetically favorable configuration of the colloid instead of perfecting lattice crystallization in a single, long event under equilibrium conditions.

Understanding noise as a factor leading to the enhanced regularity of certain oscillations, improved signal-to-noise ratio in communication channels, and induced dynamical bifurcations, gave rise to novel research directions in biology, communication systems, and semiconductor dynamics.[15–17] It was observed that noise also plays an important role in pattern formation of extended systems and, in particular, the effect of spatial coherence resonance in excitable systems was studied.[18,19] Noise-related mechanisms such as stochastic resonance,[20] coherence resonance,[21] and Brownian motors[22,23] were recently applied to improve the ordering of self-assembled structures.

Furthermore, we previously found that waves produced in a vessel containing a colloidal suspension by the air flow during crystal self-assembly enhance the opal ordering.[24] However, no systematic studies of this topic have been reported so far. In order to investigate the role of noise-like acoustic waves on the self-assembly of colloidal crystals we employed here another strategy that can be identified as acoustic field-assisted growth.[25] Applying the vibrations to the colloidal suspension using a computer-controlled setup made it possible to study changes in colloidal crystal ordering as a function of the mean vibration magnitude. Consequently, an equally important task is to find a reliable method for quantitative characterization of incremental changes in the lattice ordering, seen using scanning electron microscopy (SEM). For this, we developed a nanometrology approach that i) is robust against deficiencies of the SEM images such as uncertainties in image contrast, resolution, and focusing and ii) allows quantification of the in-plane lattice order. In order to prove the reliability of this structural analysis, we compared the results of this procedure to those produced by widely used alternative methods.

The structural data were completed by optical characterization of diffraction resonances in the opal lattice. Numerical modeling of the transmission spectra was performed to establish the reference in the form of the spectra of a perfectly ordered opal film. The lattice order improvement trend under the influence of noise agitation was observed, suggesting a correlation between SEM-visualized 2D ordering and optically detected 3D ordering. Finally, we put forth a hypothesis that assigns the noise-induced ordering of the opal lattice to spatial coherence resonance.

2. Acoustic Noise-Assisted Self-Assembly

Thin opal films were crystallized on a glass substrate that is vertically drawn out of a suspension of highly monodispersed poly(methyl metacrylate) (PMMA) spheres with diameters (D) of 368 nm and 530 nm (**Figure 1**a). Figure 1b shows the conventional schematics illustrating the crystallization process, where the spheres are brought towards the liquid/air boundary by the capillary force induced at the surface of the moving substrate.[26] The self-organization of the dense ensemble takes place around the liquid/air contact line. In our experiment acoustic vibrations in the form of white noise, with a frequency band spanning from 20 Hz to 4 kHz, were applied to the colloidal suspension during the growth process using a loud speaker fed by noise generating software (see Figure 1d). Since the substrate was suspended independently from the vessel, the contact line separating liquid and air moves with a mean magnitude that depends on the acoustic power loaded on the loud speaker. A series of opal films were grown, each under a different noise intensity level, L, measured in decibels (dB) relative to each other. The noise intensity level was calibrated with respect to the water meniscus displacement so that at $L = 20$ dB the meniscus displacement was about 2.0 μm.

Figure 2 shows SEM images of samples grown at various noise intensities. Qualitatively, we observed that for $L = 0$ dB (Figure 2a) the structure appears to be fairly irregular. For $L = 20$ dB (Figure 2c) large domains with visually almost perfect ordering are observed. At higher noise levels of $L = 25$ dB to $L = 40$ dB, the regularity of the structure monotonically declines with increasing noise intensity. At $L = 40$ dB the standing waves on the water surface dominate the wave pattern, giving rise to a spatially inhomogeneous structure of the opal film (see Figure 2g,h). These standing waves are produced by shock excitation of the eigenmodes of the beaker. The standing wave pattern manifests the faster growth of the magnitude of resonance waves compared to that of chaotic vibrations, which leads to the regular perturbation of the contact line across the substrate.

3. Assessment of Crystalline Order

To obtain a quantitative measure of the regularity of the in-plane ordering of the spheres, we carried out a statistical analysis on the SEM images. Each sample was examined based on a series of SEM images taken from 17 equidistant positions at 1 mm separation across the sample, as shown by the white dotted line in Figure 1a. A cross-sectional SEM image of the sample grown at $L = 25$ dB is shown in Figure 1c, where excellent packing and ordering of the spheres can be readily observed.

For an accurate analysis, the measure has to be: i) a scalar quantity, because a dependency on a certain predefined orientation of the sample is undesirable; ii) an average over locally observable quantities; iii) based on the positions of the center of the spheres and not on the pixel representation of the spheres in the SEM images; iv) robust against missing surface spheres; and v) suitable for cross-sample comparison.

In light of the above requirements, we introduced the function $p(r)$ as a suitable regularity measure that exploits the six-fold symmetry of the in-plane hexagonal lattice. Using the concept of the "opposite partner sphere", we defined the regularity measure as the probability of finding an opposite partner sphere (see Figure 1e). The regularity measure $p(r)$ is therefore rationally defined as:

ADVANCED FUNCTIONAL MATERIALS
www.afm-journal.de

www.MaterialsViews.com

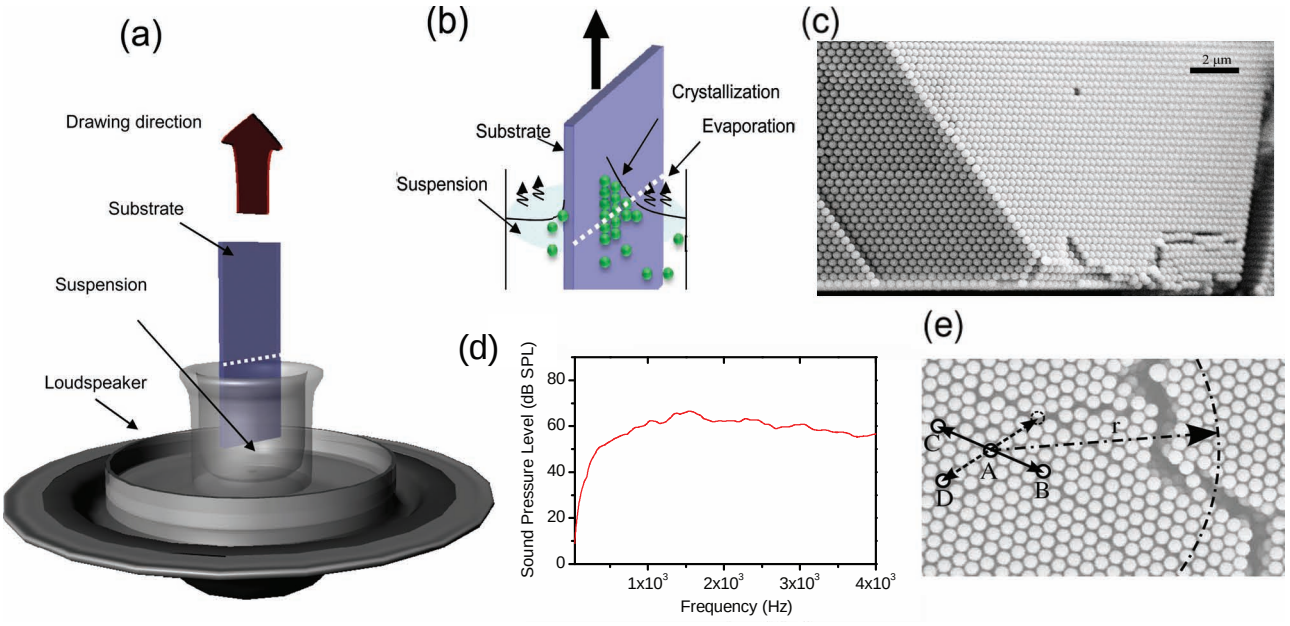

Figure 1. a) Schematics of the deposition process of a colloidal crystal from an aqueous suspension of PMMA spheres. During the growth process, acoustic vibrations with the white noise spectrum were applied from below while the substrate was vertically drawn out of the suspension by a stepper motor. b) Schematics of the crystallization process. The white dotted lines in (a) denote the line along which SEM images are taken. The same line in (b) shows the air/water contact line. c) A cross-sectional SEM image of the opal film grown at $L = 25$ dB. The scale bar is 2 μm. d) The spectrum of white noise used in the experiment. e) Illustration of the concept of the "opposite partner sphere." Sphere B has a partner sphere C that is at the opposite position with respect to the center sphere A. Sphere D does not have an opposite sphere at the position indicated by the dashed circle. The dash-dotted circle of a radius r around the sphere A indicates the range within which all the spheres are taken into account for the calculation of crystalline order at the position of the sphere A, i.e., $p_A(r)$.

$$p(r) = \frac{\sum_{A\neq B,C} \chi_r(\overrightarrow{AB})\chi_\varepsilon(\overrightarrow{AB}+\overrightarrow{AC})}{\sum_{A\neq B} \chi_r(\overrightarrow{AB})} \quad (1)$$

where $\overrightarrow{XY}$ is the vector from the center of sphere X to the center of sphere Y and $\chi_\gamma(\overrightarrow{R})$ is a characteristic function defined as:

$$\chi_\gamma(\overrightarrow{R}) = \begin{cases} 1 \text{ if } \left|\overrightarrow{R}\right| < \gamma \\ 0 \text{ else} \end{cases} \quad (2)$$

The subscripts ε and r as given in Equation 1 represent the tolerance parameters that quantify, respectively, the allowed variance in the sphere position and the maximum distance between spheres contributing to the sum in Equation 1. For the

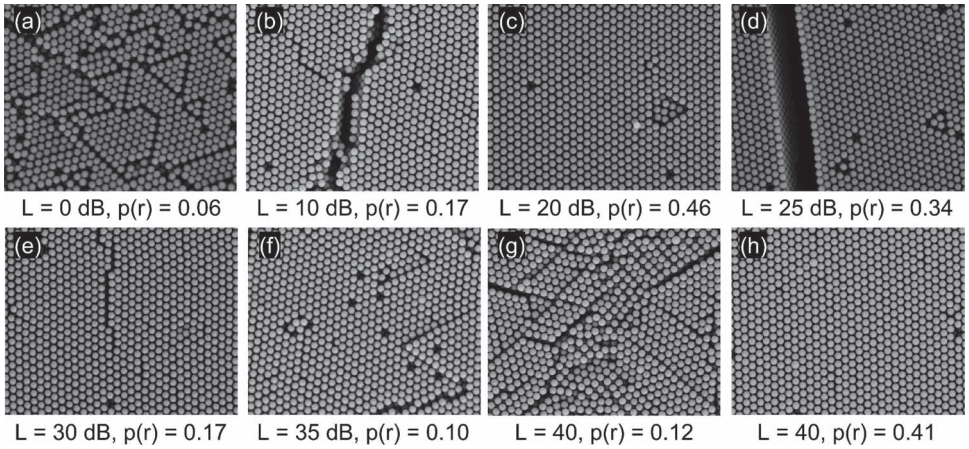

Figure 2. SEM images of samples crystallized at different noise levels L. The images in panels (a–g) are taken from equivalent spots close to the horizontal center of the samples (position 10 in the units of Figure 3). Panel (h) displays an alternative spot (position 3) for $L = 40$ dB, which shows a high regularity due to the formation of resonance standing waves at high noise intensity. p (r) denotes the regularity measure according to Equation 1 calculated from high-resolution SEM images with sizes of 65 μm × 50 μm for $r = 5.5$ μm and $\varepsilon = 43$ nm. The images are 9 μm × 9 μm in size.

case of the photonic structure exemplified here the meaningful value of r is determined by the coherence length of the incident light, which limits constructive interference over large distances, whereas ε is limited by the resolution of the SEM image.

The regularity measure $p(r)$ can be interpreted as follows: for two randomly chosen spheres A and B with the only constraint being that the distance between the respective sphere centers is less than r (i.e., $\overrightarrow{AB} < r$), $p(r)$ is defined as the probability that there exists a third sphere C such that A, B, and C are collinear and that the distance between A and B is, within the tolerance limit given by ε, the same as that between A and C; in other words, $\left|\overrightarrow{AB} + \overrightarrow{AC}\right| < \varepsilon$. This process is illustrated in Figure 1e, where the solid arrows indicate two spheres that are point-symmetric with respect to the center sphere A. The dashed arrow indicates a case where, for sphere D, there is no opposite partner.

The local regularity measure at a chosen sphere A can be defined as $p_A(r) = O_A(r)/N_A(r)$, where $O_A(r)$ is the number of spheres within a circle of radius r around the sphere A that have an opposite partner sphere and $N_A(r)$ is the total number of spheres within this circle less one, i.e., omitting the central sphere. Equation 1 can then be expressed in terms of a weighted average as follows:

$$p(r) = \frac{\sum_A N_A(r)\, p_A(r)}{\sum_A N_A(r)} \tag{3}$$

For a perfectly ordered close-packed hexagonal lattice, which is the projection of a face-centered cubic (fcc) lattice onto its (111) plane,[27] we obtain $p(r) = 1$ for all r values. For an ensemble arrangement without any long-range order $p(r)$ can be estimated assuming that the average area density is similar to the perfectly ordered case, as:

$$p(r) = \frac{2\pi}{\sqrt{3}} (\varepsilon / D)^2 \tag{4}$$

Based on a series of SEM images, we calculated $p(r)$ using $r = 5.5\ \mu m \approx 15D$, where D is the diameter, and $\varepsilon = 43$ nm $\approx 0.12D$. The results are shown in **Figure 3** as a function of noise intensity and position along the white dotted lines in Figure 1a. Details on the dependence of $p(r)$ on r and ε can be found in the Supporting Information, where we show that, for the purpose of a relative comparison of sample regularity, the exact values of r and ε are not critical.

The plots on the left-hand side of Figure 3a show $p(r)$ as a function of noise intensity for SEM images taken at position 7 and 10, i.e., around the center of the sample, which exhibits maxima of $p(r)$ at noise intensity $L = 25$ dB and $L = 20$ dB, respectively, for colloidal crystal grown with spheres of 368 nm diameter. A similar trend is observed for all positions as illustrated by the greyscale plot on the right-hand side of Figure 3a.

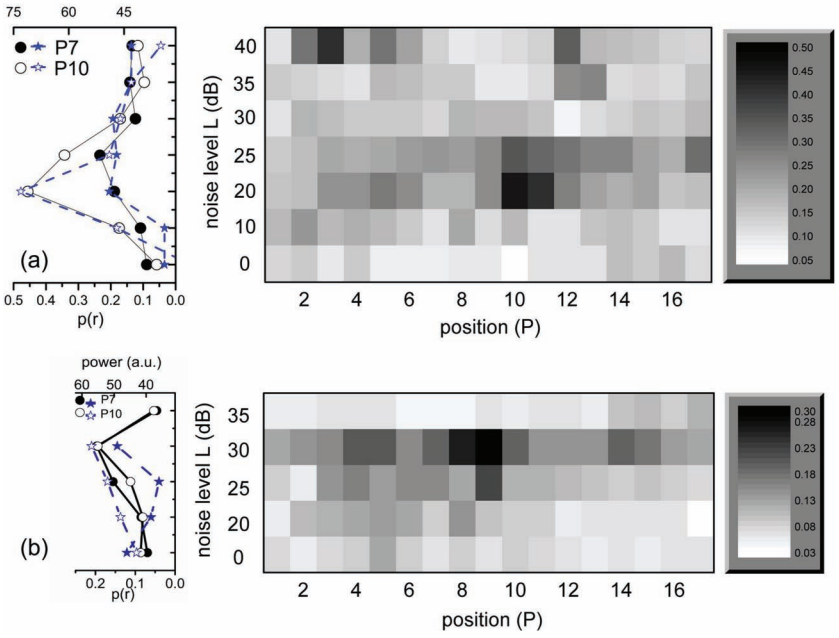

Figure 3. The regularity measure p (r) calculated according to Equation 1 for samples crystallized from spheres with diameters of a) 368 nm and b) 530 nm. The calculation parameters were $r = 5.5$ µm and $\varepsilon = 43$ nm. Left: plots of p (r) (circles) and the magnitudes of the first harmonic of PSD of the corresponding SEM images (stars) as a function of noise intensity at two locations P7 and P10. Right: plots of p (r) as a function of position P (horizontal axis) and noise level L (vertical axis). Light and dark color denotes low and high p (r) values, respectively.

The mostly light color observed for zero noise level indicates a highly irregular structure with $p(r) = 0.06$. The regularity gradually improves up to the noise level $L = 20$ dB, where a highly regular structure with $p(r) = 0.46$ is observed. A further increase in noise intensity above $L = 20$ dB leads to a decrease in regularity.

We note that the $p(r)$ value depends on the resolution of the SEM images, which limits in practice the maximum value of $p(r)$ value to around 0.5. Therefore, the $p(r)$ values presented here offer only a relative quantitative comparison. Interestingly, the minimum value of $p(r) = 0.06$ is, however, higher than the calculated value of $p(r) = 0.05$ according to Equation 4, indicating that even the least ordered sample possesses some local ordering. To test the general character of noise agitation efficiency on the opal crystallization, we repeated our analysis for spheres of the same density but a larger diameter $D = 530$ nm (Figure 3b). A trend similar to that of the smaller spheres was observed, but with the optimum noise intensity shifted upwards to $L = 30$ dB.

We compared the estimates obtained above against well-established order quantification techniques such as Fourier transform (FT) analysis, translational (pair) correlation function, and bond-orientational correlation function. The blue curves in the plots on the left-hand side of Figure 3a,b show the magnitudes of the first harmonic of the power spectral density (PSD) as a function of noise intensity for the positions P7 and P10 of the same SEM images used in the caculation of $p(r)$. The plots are in relatively good agreement with the results obtained using our "opposite partner sphere" method. A complete FT analysis of the samples and grayscale plots similar to that displayed on

the right-hand side of Figure 3 can be found in the Supporting Information.

Translational, $g(r)$, and bond-orientational, $g_6(r)$, correlation functions are obtained based on the procedure described in ref. [28]. In the case of crystalline solid, $g(r)$ obeys the power-law decay[29,30] with an algebraic form: $g(r) \propto r^{-\eta}$, where the translational exponent, η, denotes the degree of translational order in the structure with larger η denoting higher disorder.

Figure 4a shows $g(r)$ calculated for $L = 20$ dB sample along with a fit obtained using the following equation:[31]

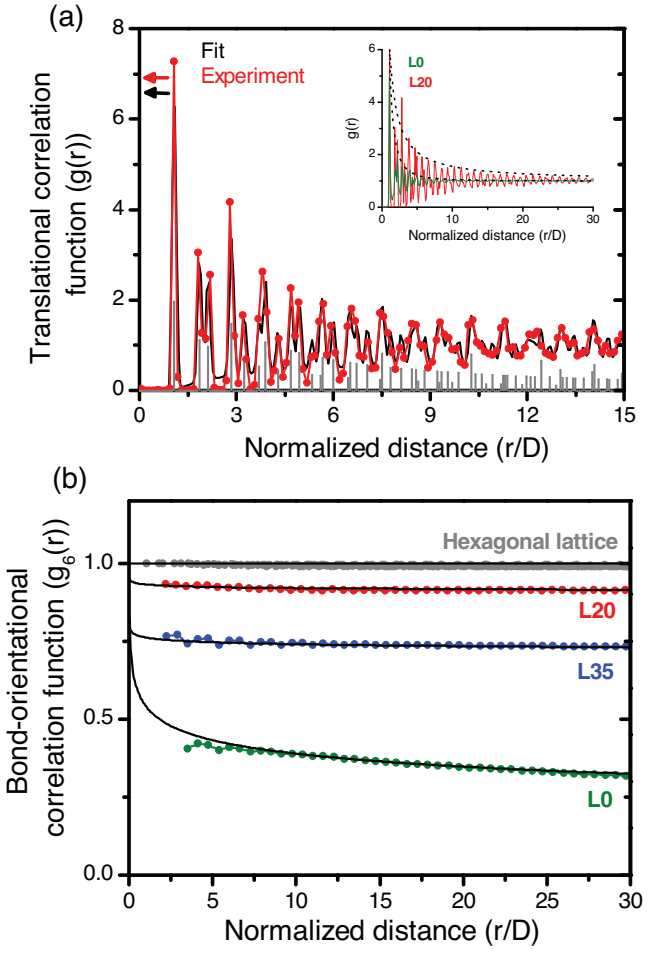

Figure 4. a) Translational correlation function $g(r)$ calculated for $L = 20$ dB sample with sphere diameter of 368 nm (red curve). The fit obtained from Equation 5 is shown by the black solid curve. The delta functions corresponding to $g_{hex}(r)$ of the perfect hexagonal lattice are shown as vertical grey lines with correct positions and relative amplitudes. Inset: Comparison of $g(r)$ calculated for $L = 0$ (green) and 20 dB (red) samples. The black dotted lines corresponds to power-law decay fits with $\eta = 2.7$ for $L = 0$ dB and $\eta = 1.4$ for $L = 20$ dB. b) Bond-orientational correlation function $g_6(r)$ calculated directly from Delauney triangulations using Equation 6 are shown for $L = 0$ (green), 20 (red), and 35 dB (blue) samples and a perfect hexagonal lattice (grey). The solid black lines are fits of the form $g_6(r) \propto r^{-\eta_6}$, yielding $\eta_6 = 0.082$, 0.006, and 0.012 for $L = 0$, 20, and 35 dB, respectively. All the calculations are based on the data at the position P10.

$$g_{fit}(r) = \left\{ \int_0^\infty g_{hex}(x, a) \exp\left[-\frac{(x-r)^2}{4b^2} \right] dx - 1 \right\} r^{-\eta} + 1 \qquad (5)$$

where $g_{hex}(x,a)$ is the translational correlation function of a perfect hexagonal lattice with lattice spacing given by a, η is the translational exponent, b is the broadening factor introduced into the delta function of the $g_{hex}(x,a)$ to account for uncertainties in sphere positions.

The fit in Figure 4a was achieved with $b \approx 0.08$ (r/D), the value of which is similar in magnitude to the tolerance parameter ε used to evaluate Equation 1. The inset to Figure 4a shows $g(r)$ calculated for $L = 0$ dB and $L = 20$ dB samples. The black dashed lines are power-law decay with $\eta = 2.7$ for $L = 0$ dB and $\eta = 1.4$ for $L = 20$ dB, respectively.

Order quantification based on the bond-orientation correlation function $g_6(r)$ is defined in terms of nearest neighbor bond angles according to ref. [28] as:

$$g_6(r) = \frac{1}{N} \sum_{i=1}^{N} \cos(6(\theta_{ij} - \theta_0)) \qquad (6)$$

where N is the number of spheres, θ_0 is the bond angle at sphere i with respect to an arbitrary fixed axis, θ_{ij} is the bond angles of the nearest neighbors of the spheres i determined directly from Delauney triangulation (see Figure S7 in the Supporting Information).

For a structure with long-range order, $g_6(r) \rightarrow$ constant, with a maximum value of unity for a perfect hexagonal lattice. For finite-range ordered structure, the magnitude of $g_6(r)$ decreases with increasing disorder and decays as a function of r.

Figure 4b shows $g_6(r)$ for $L = 0$, 20, and 35 dB samples as well as for a perfect hexagonal lattice. The bond-orientation exponents η_6 obtained from the power-law fit[29,30] are shown as grey dashed lines in the figure acquiring values of: 0.006 ($L = 20$ dB) $< \eta_6 <$ 0.082 ($L = 0$ dB). See Supporting Information for a plot of η_6 as a function of noise intensity. The small values of η_6 indicate that the samples under study have long-range order, but with a different degree of ordering towards the hexagonal lattice given by the magnitude of $g_6(r)$.

Figure 5a,b show the translational exponents and the magnitude of $g_6(r)$ extracted at $r = 15$ (r/D) as a function of noise intensity for the positions P7 and P10, respectively, so as to allow for a direct comparison with both the FT and the $p(r)$ analyses shown in Figure 3. The shaded regions indicate the spectral range of the noise intensity where the best order improvement is observed for 368 nm (green) and 530 nm (blue) spheres, respectively. The higher noise intensity associated with better order of larger spheres is in good agreement with those shown in Figure 3.

The analyses above indicate that noise indeed has a positive influence on the ordering of the spheres. In addition, the excellent agreement between the FT analysis and correlation methods with the proposed "opposite partner sphere" method justifies its validity. The advantage of our approach over the established methods is that it circumvents the problems associated with the image contrast and edge effects associated with FT analysis. In addition, our technique is also free from errors related to binning operations required in the calculation of $g(r)$ and $g_6(r)$. This error is shown to be sample-dependent, which

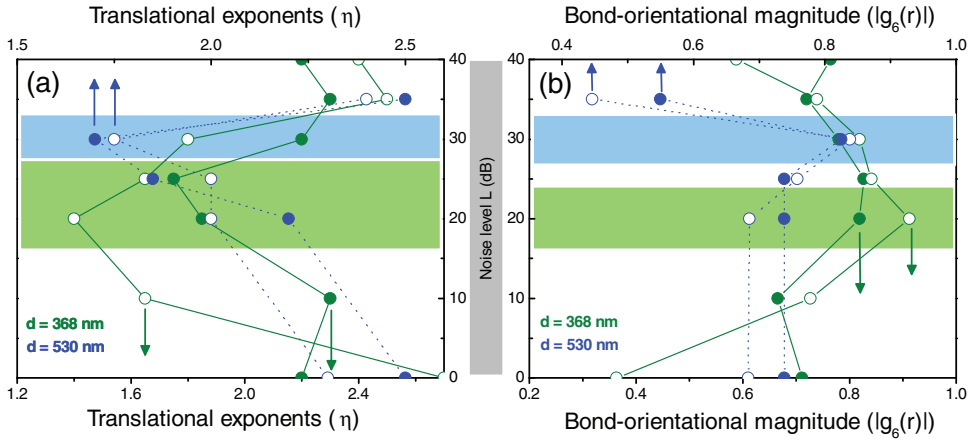

Figure 5. a) Translational exponents η obtained from the fit using Equation 5. b) Magnitude of bond-orientational correlation function extracted at $r/D = 15$. The values are plotted as a function of noise intensity for spheres diameters 368 nm (green) and 530 nm (blue). Solid circles: P7; open circles: P10.

complicates cross-sample comparison and can lead to an unreliable analysis. See Figure S10 in the Supporting Information for more details.

4. Effect of Noise on 3D Lattice Ordering

It is instructive to bridge the order estimates obtained using the surface analysis above to the optical diffraction in the respective 3D lattices obtained using angle-resolved transmission spectroscopy. The latter technique substantially extends the information about crystallographic configuration of the opal lattice in comparison to the order estimates obtained by FT analysis and correlation function calculations of the opal surface and potentially can produce a quantitative link between 2D and 3D ordering.[32]

Figure 6a shows the transmission spectra of samples grown from spheres with $D = 368$ nm at an incident angle of $\theta = 30°$ along the LU line ($\phi = 0°$, see **Figure 7**) on the surface of the Brillouin zone of an fcc lattice, where ϕ is the azimuth angle or the rotation angle of the incidence plane. The diffraction resonances at both the (111) and (002) crystal planes are more pronounced for $L = 25$ dB than for $L = 0$ dB, and the minimum at (220) is only visible for the former. This agrees with the previous observation that the diffraction resonance at the (220) planes is the most vulnerable to the lattice disorder.[32] It is also worth noting that the depth of (220) diffraction minima has been used to characterize microscale inhomogeneity of slab-shaped crystals of thermoelectric materials.[33] Furthermore, in the spectral range between these diffraction resonances the sample grown under $L = 25$ dB is more transparent. This is illustrated by the ratio of the two transmission spectra, as shown in Figure 4b. The higher transmission implies a weaker diffuse background scattering for $L = 25$ dB that can be ascribed to its better ordered lattice[34] compared to that of sample $L = 0$ dB.

The fcc lattice is a trigonal system and has a dihedral D_3 symmetry with respect to the [111] axis; it is therefore instructive to consider also the transmission spectra as a function of the azimuth angle, ϕ. We compared the contour plots of calculated total transmission spectra of an fcc lattice obtained using the transfer matrix method[35] (Figure 6c) to experimental ones (Figure 6d: $L = 25$ dB and Figure 6e: $L = 0$ dB) obtained in the zero diffraction order. As expected from the D_3 symmetry, a pronounced threefold rotational pattern is evident in the simulated transmission spectra, which was also revealed in diffraction resonance dispersion analysis of an fcc lattice.[32] The features at $\lambda = 480$ nm apparently associated to a sixfold symmetry (indicated by the dashed arrows) actually belong to threefold rotational symmetry, as follows from closer examination of their shapes. The experimentally observed sixfold symmetry can be conveniently associated with the stacking faults in the opal film lattice as recently reported by Andreani et. al.[36]

A comparison of the experimental to the calculated transmission contours indicates that the opal films grown under white noise agitation possess more regular structures: the threefold symmetry is hardly detected for $L = 0$ dB (Figure 6e), while features with threefold rotational symmetry can be clearly observed in the pattern for $L = 25$ dB sample (Figure 6d). Since the diffraction resonances at short wavelengths belong to high-index planes, it is reasonable to assume that lattice disorder affects them more strongly than the diffraction resonances at low-index lattice planes.[37] Therefore, the sample with better order should display symmetry of diffraction resonances at shorter wavelengths. Indeed, the transmission pattern of the opal film crystallized under noise agitation also shows distinguishable sixfold and 12-fold symmetries. However, the 12-fold symmetry at $\lambda \approx 380$ nm has no matching features in the calculated transmission contour. This is a consequence of integrating the zero and the higher diffracted orders in the calculated total transmission spectra. Altogether, these observations support the conclusion that noise agitation improves the lattice ordering.

5. Role of Noise Agitation

It has been known for more than a century that noise in the form of thermal atomic motion plays a crucial role in phase

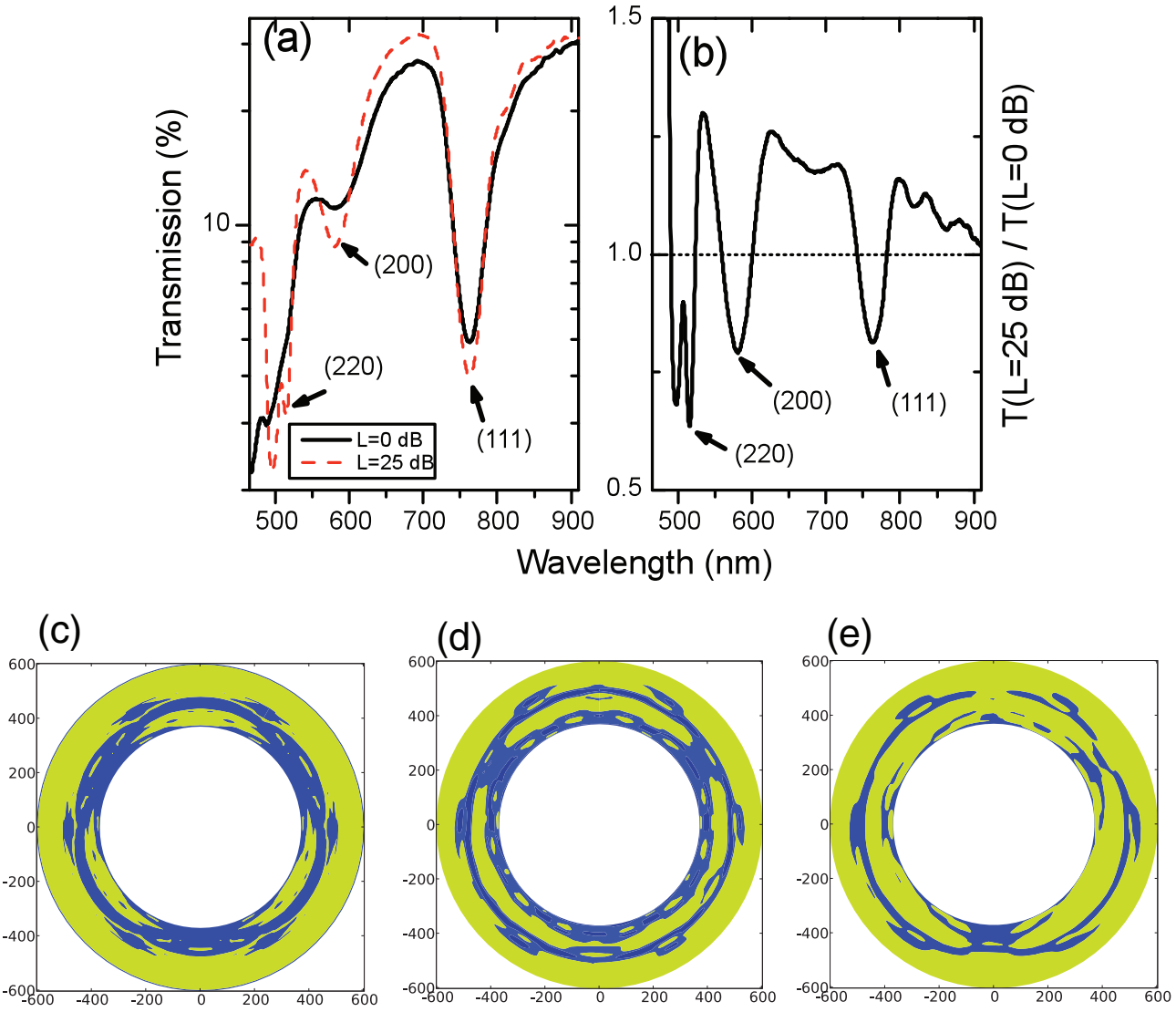

Figure 6. a) Optical transmission spectra obtained at an angle of incidence $\theta = 30°$ and $\alpha = 0°$ for $L = 0$ dB (black solid line) and $L = 25$ dB samples (dashed red line) ($D = 368$ nm). b) The ratio of these two spectra: T ($L = 25$ dB)/T ($L = 0$dB). Contour plots of transmission spectra obtained at an incident angle of $\theta = 30°$ as a function of wavelength and the azimuth angle, ϕ: c) from calculations for opal with an exact fcc lattice, d) experimental data for the sample grown at $L = 25$ dB, and e) experimental data for the sample grown at $L = 0$ dB. The calculation was performed using the same material and structure parameters as in the experiment.

transitions.[38] The effect of noise in such cases can be described by a locally defined effective temperature, which is adiabatically adjusted and varied very slowly on the atomic length scale. Therefore, the classical annealing process can be described in the framework of adiabatic equilibrium thermodynamics using a locally defined Gibb's free energy and a locally defined effective temperature. Based on this analogy, researchers often seek to improve the crystallization of colloidal suspension by changing the bath temperature, introducing electrolytes, or using solvents with higher vapor pressures.[39] These approaches assume equilibrium crystallization of charged particles,[40,41] and they are proven to yield better ordering in the opal lattice. However, none of these methods considered waves in the water or on its surface.

On the contrary, comparing freely moving particles in a colloidal suspension to the same particles frozen at lattice nodes of a crystallized film, a reasonable assumption would be that crystallization drives the system out of equilibrium. How do we bridge this approach to noise-enhanced spatial regularity?[42]

An illustrative analogy to wave-driven colloidal sphere packaging is the arrangement of sand particles under the influence of water waves coming to the beach. In this case, not only the kinetic energy of the waves is transferred to sand particles, but also the Archimedes force counteracting the gravity makes them susceptible to the driving force. The wave essentially provides a correlated movement of the sand particles. Moreover, if one wants to change an established configuration, the magnitude of the wave should be high enough to allow destructive

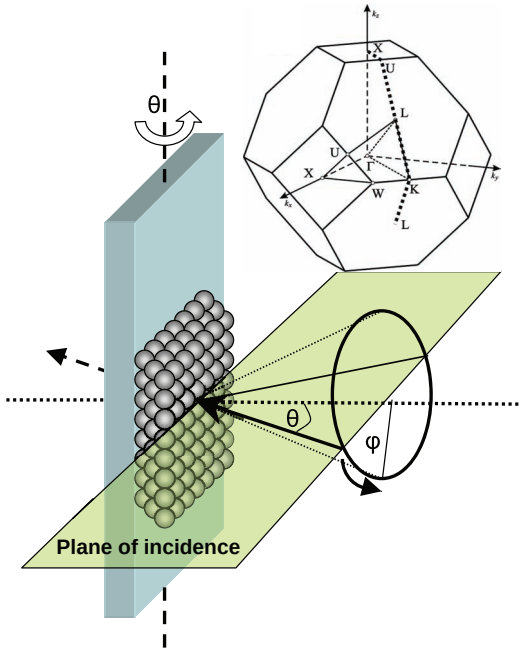

Figure 7. Schematic of transmission measurement. The inset shows the first Brillouin zone of an fcc lattice, where the dotted line indicates the plane of incidence.

forces to overcome the interaction between sand particles at the edge between dry and wet parts. To come closer to opal crystallization, gravity should be replaced with van der Waals forces cementing the sphere package. Taking into account the electrostatic nature of van der Waals forces and the porosity of the sphere sediment, the role of the water wave is to shield sporadically the electrostatic interaction between spheres and to give them some freedom to couple to the wave energy, thus allowing changes in their positions in order to minimize the package energy.

Since the crystallization of colloidal spheres takes place at the meniscus on the substrate,[26] the observed influence of noise is confined to this region. The total flux of water in the meniscus region in the case of meniscus perturbation is mainly the sum of two terms: the evaporation-induced flux of water and the oscillating flux of water.[26,43] The oscillating fraction of flux corresponds to the agitation frequency. In fact, the drawing speed is ≈0.38 μm s^{-1}, which is about one lattice spacing every 1.5 s in crystals assembled from 368 nm spheres, whereas the oscillation frequency of the water flux can be up to 3000 cycles in every 1.5 s. This frequent movement of the water level across the contact line either releases spheres from lattice sites or allows them to be captured deeper into the potential well. This freedom increases the probability for spheres to find the most energetically favorable lodging sites.[43,44]

Once the sphere is captured in the deepest potential well, a stronger perturbation is necessary to release it back to the suspension. Since this external perturbation is reduced along the substrate being drawn out of the suspension, the balance between capture and release forces is shifted in favor of the lattice perfection above the contact line.

It is also instructive to introduce here the concept of "colloidal epitaxy". Assuming that the solidified part of the opal lattice acquires a "perfect" order, the softening of the lattice in close vicinity to the crystals allows van der Waals forces to replicate this perfection in the next cross-cut of sphere lattice by equalizing interaction between spheres. Thus, the application of water waves allows the epitaxy process to repeat the crystallization process several times for the same cross-cut, which promotes order in the ensemble.

Obviously, the acoustic energy injected into the system will be partly dissipated into other degrees of freedom such as heat. Therefore, one could argue that it is the thermal gradient thus formed that drives the spheres in suspension. However, the thermal motion is different from that generated by noise agitation. By changing the temperature, each sphere is pushed individually through collisions with other spheres in the surrounding water bath. There is no significant correlation in the motion of the spheres and no large-scale density fluctuation due to temperature change unless the water starts to boil. Furthermore, the propagation of heat is governed by heat equation and its dynamics is fundamentally different from the wave equation since, in particular, the former does not allow for wave excitation.

The effect of acoustic waves is to provide correlated movements of the spheres, which make the crystal order a function of the vibrational magnitude. We note that, such meniscus movement could be considered analogous to shear-enhanced crystallization.[45–47] The most ordered lattice were achieved at agitation level of L = 20 and 30 dB in suspensions of 368 and 530 nm spheres, respectively. These agitation magnitudes result in water meniscus displacements that correspond to three and five times the respective lattice constants. This observation suggests that there exists an optimum displacement of the water surface for the spheres to find the right lattice positions under "melting–freezing" conditions. Certainly, the optimum value is a function of the water evaporation rate, the substrate drawing speed, and the weight of the spheres. Since the first two parameters were maintained as constant in our experiment, the larger spheres require stronger agitation to achieve lattice alignment. Under very high agitation intensity the wave magnitude strongly exceeds the lattice constant so that the lattice is melted simultaneously over the length of many unit cells. Such a high disturbance destroys the regime of "colloidal epitaxy." As a consequence, under- or over-agitation will eventually result in a less-ordered lattice.

What is the role of the acoustic noise in crystal ordering? First, the acoustic agitation allows multiple crystallization attempts, i.e., it provides the reversibility of the crystallization process that is an essential condition for the stochastic resonance to occur. Second, it is noteworthy that in the range $f \leq 4$ kHz ($\lambda \geq 0.375$ m) the sound speed in water allows all acoustic waves to move the suspension as a whole. As a result, a complex wave pattern is formed on the surface of the liquid because each partial wave approaches the surface with its own phase. The energy delivered with each partial frequency depends on the wave phase at the contact line. Accordingly, the concept of stochastic resonance assumes that high waves are able to switch between the ensemble configurations, whereas the bunch of low amplitude waves promote the aforementioned

switching through which the role of noise is manifested. This is why the actual noise spectrum is irrelevant, but the application of noise agitation is essential because it provides a complex wave superposition irrespective of the size and shape of the vessel. Since the vibrations of the water level at the contact line are translated into melting and assembling of the colloidal crystal, the crystallization and melting of the opal lattice is synchronized by the highest wave along the contact line. Overall, such a process makes the final ordering of the whole system, on average, better than any single realization of order.

It is worth noting that in the case of monochromatic agitation one has to adjust both the magnitude and frequency of the acoustic wave to reach the optimum order, but the contribution of the stochastic resonance will be lost. Investigation of such regime of agitation is also of interest but it is outside the scope of this paper.

6. Conclusions

The major result of our work is the demonstration of the mechanical approach to the crystallization of the opal lattice in a moving meniscus. Traditional approaches often focus on maintaining the adiabatic transition between the almost-melted and almost-crystallized colloids by maintaining the system in equilibrium. Instead, smashing the crystallization continuity by frequent transitions from melted to frozen lattice states brings a valuable opportunity to the lattice order improvement. Important observation is the optimum level of acoustic noise leading to better order, which demonstrates the possibility to control noise-assisted crystallization. What is more advantageous: to build up the opal lattice at once using long adiabatic transition or to use thousands of tries hoping that each of the tries incrementally improves the ordering? To answer this question a number of criteria have yet to be elaborated. Obviously, for mass production, the most cost-efficient approach will be a winning option. Apparently, the noise agitation can be viewed as a "quick-and-dirty" mechanical alternative to the precise chemically controlled equilibrium crystallization.

The mechanism of noise-assisted lattice crystallization can be treated in terms of the spatial coherence resonance. Our findings demonstrate a practical and beneficial example of the constructive role of noise in a crystallization process of self-organized opal films. We believe an opportunity exists for self-assembly under spatial coherence resonance-like conditions to be applied to nanostructures with other length scales provided the mechanical force is comparable to, e.g., electrostatic, magnetic, capillary forces, or van der Waals forces.

Significant progress was made in the development of a quantitative order measure based on the "opposite partner" concept. The measure was applied to determine the ordering of the (111) plane of opal films crystallized under acoustic agitation of the sphere suspension. We checked the results of our concept against commonly used techniques of FT and translational and bond-orientational correlation functions. Excellent agreement was obtained that justifies the applicability of the concept. Moreover, our proposed measure offers advantages of i) robustness against image contrast variation and edge effects that undermine the FT technique, ii) reliability of cross-sample comparison, and iii) avoidance of binning error associated with the correlation functions. Furthermore, analysis of the rotation symmetry of diffraction resonances from high-index crystal planes in measured and calculated optical transmission spectra supported the correlation between surface and volume ordering of opal films.

7. Experimental Section

Materials: The highly monodisperse PMMA spheres were prepared with a median diameter of D = 368 nm and 530 nm by the modified surfactant-free emulsion polymerization technique.[48] The opal films were self-assembled on glass substrates from a 4 wt% dispersion of PMMA spheres in deionized water with a resistivity of 18 MΩ cm. The substrate was vertically drawn out of the suspension using a stepper motor with a typical speed of 1.35 mm h^{-1} at controlled temperature and humidity levels of 25 °C ± 2 °C and 23% ± 3%, respectively. The resulting opal films typically possess the thickness of about 80 (111) layers of spheres over an area of about 400 mm^2.

Meniscus Displacement Measurement: The root mean square (rms) displacement of the water surface was measured using an optically generated dual-cavity Fabry–Pérot interferometer with the modified fringe-counting technique.[49] In principle, any change in the optical path length of the cavity iss reflected in a phase change of the laser beam. The phase change causes the reference and reflected signals to interfere, thereby modulating the detected signal intensity. By counting the fringes in the interference pattern, information about the displacement of the water surface was obtained. In the experiment a laser diode with a wavelength of 1310 nm was used. A microprismatic-type retroreflector was employed as the target, which was suspended at a fixed location from the water surface. Due to the scattering of laser light at the water/air interface, the resolution of the measurement is limited to 0.65 μm.

Coordinate Determination Technique: The extraction of the coordinates of the spheres from the SEM images was based on calculating a convolution of the original images with a matrix that is sensitive to the borders of the spheres. A list of $\vec{r}_i$ of the 2D coordinates of the centers of the spheres was then obtained by extracting the positions of the local maxima in the convoluted image. The method identifies more than 99% of the spheres with accuracy in the coordinates of about 20 nm, which depends on the resolution of the SEM images.

Transmission Spectroscopy: Transmission measurements were performed with the white light from a halogen lamp, collimated into a parallel beam with a diameter of ≈1 mm using an optical telescope. Samples were mounted on a five-axis rotation stage that allowed independent adjustment of the incident angle, θ, and the azimuth angle, ϕ (Figure 7). The transmitted light was collected with a collection angle of approximately 3° and registered by a broadband high-resolution charge-coupled detector (CCD) spectrometer. The (*hkl*) diffraction resonances are assigned according to the Bragg Law: $\lambda = 2 * n_{\text{eff}} d_{hkl} \sqrt{(1 - \sin^2(\alpha_{hkl}))}$, where d_{hkl} is the interplanar distance of the (*hkl*) planes, n_{eff} is the effective index of refraction, and α_{hkl} is the angle between the incident light and the normal vector to the (*hkl*) lattice planes. The n_{eff} = 1.37 was obtained as fitting parameter from the Bragg fit to the experimental dispersion of the diffraction resonance at the (111) growth planes.[32]

Transmission Calculation: The calculated transmission contours presented in Figure 6c were obtained using the freely distributed MULTEM2 software package.[35] Input parameters were: fcc lattice with D = 368 nm, a dielectric constant of 2.15, and 96 layers thick.

Supporting Information

Supporting Information is available from the Wiley Online Library or from the author.

Acknowledgements

The authors thank Profs. Luca Gammaitoni and Lucio C. Andreani for helpful discussions. This work was supported by the Science Foundation Ireland (SFI), the EU Network of Excellence "PhOREMOST", the Irish Research Council for Science, Engineering and Technology (IRCSET), and by the Spanish MICINN (project ACPHIN FIS2009-10150). S.P. acknowledges a PhD scholarship from the Royal Thai Government.

Received: October 28, 2011
Published online: February 9, 2012

[1] Y. Xia, B. Gates, Y. Yin, Y. Lu, *Adv. Mater.* **2000**, *12*, 693.
[2] G. A. Ozin, S. M. Yang, *Adv. Funct. Mater.* **2001**, *11*, 95.
[3] A. F. Koenderink, P. M. Johnson, J. F. Galisteo Lopez, W. L. Vos, *C. R. Phys.* **2002**, *3*, 67.
[4] K. A. Arpin, A. Mihi, H. T. Johnson, A. J. Baca, J. A. Rogers, J. A. Lewis, P. V. Braun, *Adv. Mater.* **2010**, *22*, 1084.
[5] J. H. Holtz, S. A. Asher, *Nature* **2003**, *389*, 829.
[6] Y. Nishijima, K. Ueno, S. Juodkazis, V. Mizeikis, H. Misawa, T. Tanimura, K. Maeda, *Opt. Express* **2007**, *15*, 12979.
[7] X. Yu, L. Shi, D. Han, J. Zi, P. V. Braun, *Adv. Funct. Mater.* **2010**, *20*, 1910.
[8] P. Bermel, C. Luo, L. Zeng, L. C. Kimerling, J. D. Joannopoulos, *Opt. Express* **2007**, *15*, 16986.
[9] P. G. O'Brien, N. P. Kherani, A. Chutinan, G. A. Ozin, S. John, S. Zukotynski, *Adv. Mater.* **2008**, *20*, 1577.
[10] S. Guldin, S. Hüttner, M. Kolle, M. E. Welland, P. Müller-Buschbaum, R. H. Friend, U. Steiner, N. Tétreault, *Nano Lett.* **2010**, *10*, 2303.
[11] S. Arpiainen, F. Jonsson, J. R. Dekker, G. Kocher, W. Khunsin, C. M. Sotomayor Torres, J. Ahopelto, *Adv. Funct. Mater.* **2009**, *19*, 1247.
[12] Y. A. Vlasov, V. N. Astratov, A. V. Baryshev, A. A. Kaplyanskii, O. Z. Karimov, M. F. Limonov, *Phys. Rev. E* **2000**, *61*, 5784.
[13] M. Egen, R. Zentel, *Chem. Mater.* **2002**, *14*, 2176.
[14] Z.-Y. Li, Z. Q. Zhang, *Phys. Rev. B.* **2000**, *62*, 1516.
[15] D. F. Russell, L. A. Wilkenks, F. Moss, *Nature* **1999**, *402*, 291.
[16] V. S. Anishchenko, M. A. Safonova, L. O. Chua, *Int. J. Bifurcation Chaos* **1994**, *4*, 441.
[17] J. Hizanidis, A. G. Balanov, A. Amann, E. Schöll, *Phys. Rev. Lett.* **2006**, *96*, 244104.
[18] M. Perc, *Phys. Rev. E* **2005**, *72*, 016207.
[19] O. Carrillo, M. A. Santos, J. Garcia-Ojalvo, J. M. Sancho, *Europhys. Lett.* **2004**, *65*, 452.
[20] L. Gammaitoni, P. Hänggi, P. Jung, F. Marchesoni, *Rev. Mod. Phys.* **1998**, *70*, 223.
[21] A. S. Pikovsky, J. Kurths, *Phys. Rev. Lett.* **1997**, *78*, 775.
[22] R. D. Astumian, *Science* **1997**, *276*, 917.
[23] P. Reimann, *Phys. Rep.* **2002**, *361*, 57.
[24] N. Gaponik, A. Eychmüller, A. L. Rogach, V. G. Solovyev, C. M. Sotomayor Torres, S. G. Romanov, *J. Appl. Phys.* **2004**, *95*, 1029.
[25] A. Amann, W. Khunsin, G. Kocher, C. M. Sotomayor Torres, E. P. O'Reilly, *Proc. SPIE* **2007**, *6603*, 660321.
[26] N. D. Denkov, O. D. Velev, P. A. Kralchevsky, I. B. Ivanov, H. Yoshimura, K. Nagayama, *Langmuir* **1992**, *8*, 3183.
[27] P. N. Pusey, W. van Megen, P. Bartlett, B. J. Ackerson, J. G. Rarity, S. M. Underwood, *Phys. Rev. Lett.* **1989**, *63*, 2753.
[28] R. A. Quinn, C. Cui, J. Goree, J. B. Pieper, H. Thomas, G. E. Morfill, *Phys. Rev. E* **1996**, *53*, R2049.
[29] D. R. Nelson, B. I. Halperin, *Phys. Rev. B* **1978**, *19*, 2457.
[30] D. G. Grier, C. A. Murray, C. A. Bolle, P. L. Gammel, D. J. Bishop, D. B. Mitzi, A. Kapitulnik, *Phys. Rev. Lett.* **1991**, *66*, 2270.
[31] D. G. Grier, C. A. Murray, *J. Chem. Phys.* **1994**, *100*, 9088.
[32] W. Khunsin, G. Kocher, S. G. Romanov, C. M. Sotomayor Torres, *Adv. Funct. Mater.* **2008**, *18*, 2471.
[33] V. T. Bublik, V. V. Karataev, V. B. Osvenski, T. B. Sagalova, V. B. Ufimtsev, A. M. Frolov, *Proc. 16th Int. Conf. Thermoelectron.* **1997**, pp. 118–121.
[34] S. G. Romanov, C. M. Sotomayor Torres, *Phys. Rev. E* **2004**, *69*, 046611.
[35] N. Stefanou, V. Yannopapas, A. Modinos, *Comput. Phys. Commun.* **2000**, *132*, 189.
[36] L. C. Andreani, A. Balestreri, J. F. Galisteo-Lopez, M. Galli, M. Patrini, E. Descrovi, A. Chiodoni, F. Giorgis, L. Pallavidino, F. Geobaldo, *Phys. Rev. B* **2008**, *78*, 205304.
[37] W. Khunsin, S. G. Romanov, C. M. Sotomayor Torres, J. Ye, R. Zentel, *J. Appl. Phys.* **2008**, *104*, 013527.
[38] F. Reif, *Fundamental of Statistical and Thermal Physics*; McGraw-Hill, Tokyo, Japan **1965**.
[39] D. V. Kalinin, V. V. Serdobintseva, A. F. Danilyuk, S. V. Vosel, N. A. Rudina, *React. Kinet. Catal. Lett.* **2003**, *80*, 89.
[40] D. V. Kalinin, J. V. Kuznetsova, V. V. Serdobintseva, *React. Kinet. Catal. Lett.* **2003**, *78*, 291.
[41] J. F. Galisteo-López, M. Ibisate, R. Sapienza, L. S. Froufe-Pérez, Á. Blanco, C. López, *Adv. Mater.* **2011**, *23*, 30.
[42] T. Shinbrot, F. J. Muzzio, *Nature* **2001**, *410*, 251.
[43] L. Cademartiri, A. Sutti, G. Calestani, C. Dionigi, P. Nozar, A. Migliori, *Langmuir* **2003**, *19*, 7944.
[44] P. N. Pusey, W. van Megen, *Nature* **1986**, *320*, 340.
[45] B. J. Ackerson, P. N. Pusey, *Phys. Rev. Lett.* **1988**, *61*, 1033.
[46] M. D. Haw, W. C. K. Poon, P. N. Pusey, *Phys. Rev. E* **1998**, *57*, 6859.
[47] O. L. J. Pursiainen, J. J. Baumberg, H. Winkler, B. Viel, P. Spahn, T. Ruhl, *Adv. Mater.* **2008**, *20*, 1484.
[48] M. Müller, R. Zentel, T. Maka, S. G. Romanov, *Chem. Mater.* **2000**, *12*, 2508.
[49] S. Pullteap, H. C. Seat, T. Bosch, *Opt. Eng.* **2007**, *46*, 115603.